



# Strong ground motion characteristics of the 2022 $M_W$ 6.6 Luding earthquake and regional variability in ground motion among three earthquake areas in Sichuan, Southwest China

Bin Zhang<sup>1,2</sup> · Xiaojun Li<sup>3</sup> · Yanxiang Yu<sup>4</sup> · Xiaojian Lu<sup>1</sup> · Mianshui Rong<sup>3</sup> · Su Chen<sup>3</sup> · Zhao An<sup>4</sup> · Zhenghui Xiong<sup>5</sup>

Received: 19 December 2023 / Accepted: 8 May 2024 / Published online: 17 June 2024  
© The Author(s), under exclusive licence to Springer Nature B.V. 2024

## Abstract

This paper analyzed the strong motion characteristics based on 86 three-component strong motion records of the  $M_W$  6.6 Luding earthquake. Additionally, the factors that influence the variation in ground motion for three earthquakes with similar magnitude in Sichuan Province were investigated. The analysis result indicates a strong correlation between the observed ground motion parameters and the distribution of published Modified Mercalli Intensity. The residual analysis reveals that the spectral accelerations at periods 0.1–10.0 s are amplified to 0.0798–0.3057 times the mean level in the rupture forward direction and weakened to 0.0738–0.2831 times the mean level in the rupture backward direction. The maximum pulse direction recorded by the 51LDJ station is N6°E, aligning with the vertical fault direction. The velocity pulses has distinct bidirectional pulses in the waveforms, with a PGV of 37.0 cm/s. The source effect of the strike-slip  $M_W$  6.6 Luding and  $M_W$  6.5 Jiuzhaigou earthquakes on ground motion is relatively less significant compared to the average level of mainshocks in southwest China. However, the thrust-fault  $M_W$  6.7 Lushan earthquake exhibits a stronger source effect on ground motion during short and medium periods, but a weaker source effect during long periods when compared to the average level. The anelastic attenuation of the Longmenshan, Xianshuihe, and Huya fault zones in Sichuan exhibits significant regional variation and periodic correlation. This phenomenon is closely linked to the regional tectonic background variations and the heterogeneity of crustal structure within the area.

**Keywords**  $M_W$  6.6 Luding earthquake · Strong motion characteristics · Directivity effect · GMPE · Regional variability

## 1 Introduction

According to the China Earthquake Networks (CENC) (<http://www.cenc.ac.cn/>), an earthquake with magnitude  $M_W$  6.6 (or  $M_S$  6.8) occurred in Moxi Town, Luding County, Sichuan Province, at 04:52 UTC (12:52 Beijing time) on 5 September 2022. The epicenter was located at 29.59°N, 102.08°E, with a focal depth of 16 km. As of 17:00 UTC on 11 September 2022, the mainshock had resulted in the loss of 93 people, with 25 people reported missing, and over 260 people injured. This earthquake represents the most significant seismic event in terms of damage on the Chinese mainland since 2014. The findings by Zhang et al. (2023) indicate that the rupture process of this mainshock unveiled its nature as a strike-slip fault event, characterized by a rupture length of approximately 35 km. Moreover, the dominant direction of the rupture was identified as south-southeast. This earthquake occurred at the southern end of the Xianshuihe fault zone, situated within the triple-junction region where the Xianshuihe, Anninghe, and Longmenshan fault zones intersect (Yi et al. 2023). During the Luding earthquake, the National Strong Motion Observation Network System (NSMONS) of China obtained 63 three-component strong motion records from free-field stations. Additionally, the Earthquake Early Warning Network (EEWN) of Sichuan captured 23 three-component strong motion records from free-field basic stations. The distribution of the epicenter and the triggered stations is shown in Fig. 1.

During the earthquake, the distinct characteristics of ground motion often result in varying patterns of structure damage in near-fault area. Olsen et al. (2006) and Graves et al. (2008) modeled the earthquake field in the Los Angeles Basin, based on identified active faults. They discovered that the earthquake intensity in the Los Angeles region can fluctuate by an order of magnitude depending on the direction of fault rupture, whether from south to north or north to south, respectively. The study of the Kumamoto  $M_W$ 7.0 earthquake in Japan revealed that the near-fault long-period ground motion experienced significantly amplification due to the directivity effect (Xie et al. 2017). Specifically, the long-period ground motions in the rupture forward direction of the Kumamoto earthquake are much higher than average, with PGV and long-period SAs ranging from 1.2 to 1.5 times the average values. Therefore, a comprehensive analysis of ground motion observation characteristics proves instrumental in advancing our understanding of earthquake-induced damage.

In this study, based on the 86 three-component strong motion records obtained by the NSMONS and EEWN, we first analyze the characteristics of near-fault ground motion amplitude and acceleration response spectra. We then proceed to examine the spatial distribution of horizontal ground motions. Subsequently, the residual is used to evaluate and quantify the difference in horizontal ground motion between the rupture forward (south-southeast of the epicenter) and rupture backward (north-northwest of the epicenter) directions. Then the pulse-like feature of near-fault ground motion is investigated. Furthermore, we utilize the recently developed ground motion prediction equation (GMPE) for southwest China, referred to ZYLW22 (Zhang et al. 2022), to assess whether the  $M_W$  6.6 Luding earthquake conforms to the ground motion attenuation characteristics observed in the mainshocks of southwest China. Finally, we conduct residual analysis using the ZYLW22 GMPE on the 2013  $M_W$  6.7 Lushan earthquake, the 2017  $M_W$  6.5 Jiuzhaigou earthquake, and the 2022  $M_W$  6.6 Luding earthquake in Sichuan Province, southwest China. The aim of this analysis is to explore the factors influencing the variation in ground motion among

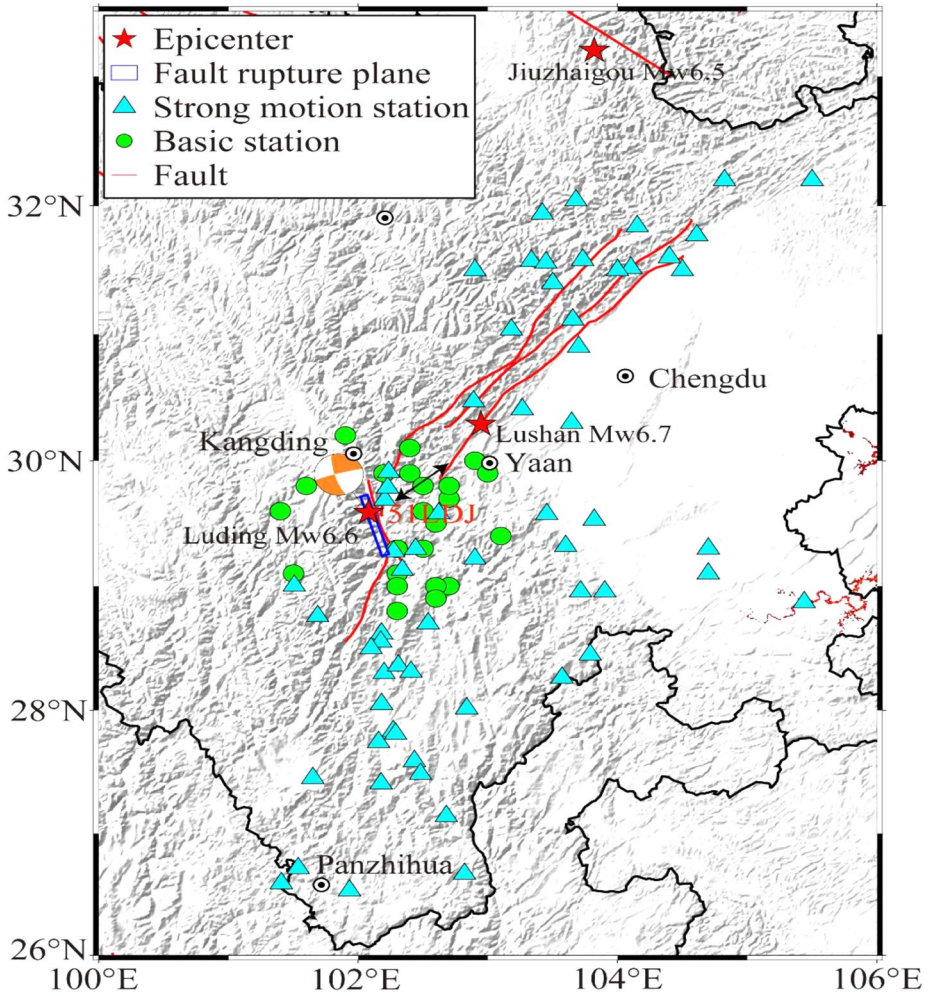


**Fig. 1** Location of recording stations and epicenters of the  $M_w$  6.6 Luding earthquake. Triangles indicate the strong motion stations in the NSMONS; Circles indicate the basic stations in the EEWN; Red stars indicate the epicenters; Blue box indicates the fault rupture plane

three strong earthquake areas within Sichuan Province, characterized by similar moment magnitude.

## 2 Observed strong ground motion

### 2.1 Dataset and data processing

The 63 three-component free-field records obtained by the NSMONS were captured by 3-component force balance accelerometers with a full-scale range of  $\pm 2$  g and a sampling rate of 200 samples/sec. The 23 three-component free-field strong motion records obtained

by the EEWN were recorded by 3-component force balance accelerometers with a full-scale range of  $\pm 2$  g and a sampling rate of 100 samples/sec. The site classification was conducted based on the time-average shear-wave velocity in the upper 30 m ( $V_{S30}$ ). For the NSMONS stations, the site  $V_{S30}$  was derived from the borehole shear-wave velocity data, as outlined in the research by Xie et al. (2022). However, since the EEWN stations lacked access to borehole shear-wave velocity data, the site  $V_{S30}$  for these stations was estimated using the relationship between the topographic slope and  $V_{S30}$  proposed by Allen and Wald (2009). The site  $V_{S30}$  for the 86 stations is presented in Table S1, with 39 stations classified as Class D sites, 42 stations as Class C sites, and 5 stations as Class B sites according to the NEHRP site classification (Wills et al. 2000). All acceleration records were subjected to a 4th-order Butterworth acausal (2-pass) bandpass filtering using the PEER-NGA data processing flow (Ancheta et al. 2013), with a low-pass cut-off frequency of 100 Hz. To ensure the reliability of the determined high-pass cut-off frequency ( $f_{hp}$ ), a series of evaluation steps were carried out, as illustrated in Zhang et al. (2022). Based on the determined  $f_{hp}$ , filtering order ( $n=4$ ), and filtering response type, the available period range for each processed record was selected according to  $1/(1.25 \times f_{hp})$  (Boore and Bommer 2005). In this study, the maximum available periods for all records were up to 10 s. Following the finite fault model of the  $M_w$  6.6 Luding earthquake (Zhang et al. 2023), as depicted in Fig. 1, we employed the method proposed by Kaklamanos et al. (2011) to calculate the rupture distance ( $R_{rup}$ ), Joyner-Boore distance ( $R_{jb}$ ), and the depth from the surface to the top of fault rupture plane ( $Z_{TOR}$ ). The rupture dimensions of the  $M_w$  6.6 Luding earthquake are provided in Table 1. Additionally, comprehensive information regarding the focal information, site information, and processed ground motion parameters of the Luding earthquake can be found in Table S1.

## 2.2 Time histories and acceleration response spectra of near-fault recordings

Among the available 86 three-component strong motion data, the maximum peak ground acceleration (PGA) was recorded at station 51SMM with a rupture distance of 27.27 km. The PGAs and peak ground velocities (PGVs) in East-West (EW), North-South (NS), and Up-Down (UD) components are  $-394.67$  gal,  $-284.73$  gal,  $114.31$  gal; and  $-12.53$  cm/s,  $9.31$  cm/s,  $4.57$  cm/s, respectively. The second-largest PGA was obtained at station 51LDJ, located at a rupture distance of 12.87 km. The PGAs and PGVs in EW, NS, and UD directions for this station are  $118.87$  gal,  $-316.00$  gal,  $160.00$  gal; and  $-12.83$  cm/s,  $37.59$  cm/s,  $-7.74$  cm/s, respectively. The third-largest PGA was recorded at station 51LDL, positioned at a rupture distance of 18.95 km. The PGAs and PGVs in EW, NS, and UD directions for this station are  $301.98$  gal,  $-193.75$  gal,  $-203.09$  gal; and  $12.48$  cm/s,  $-12.05$  cm/s,  $-6.06$  cm/s,

**Table 1** The rupture dimensions of the  $M_w$  6.6 Luding earthquake

| Model parameters                      | The finite fault model of Zhang et al. (2023) |
|---------------------------------------|---|
| Rupture area (L×W) (km <sup>2</sup> ) | 35×18   |
| Strike angle (°)                      | 163   |
| Dip angle (°)                         | 77  |
| Rake angle (°)                        | -5  |
| $Z_{TOR}$ (km)                        | 4.3   |

respectively. Table 2 presents the ground motion and site parameters for recording stations located at rupture distances less than 50 km, all situated in class C or D sites. Figure 2 illustrates the acceleration, velocity time histories, and 5% damping acceleration response spectra recorded by stations 51SMM, 51LDJ, and 51LDL. In Fig. 2d, it can be observed that the spectral accelerations (SAs) in the NS component at the 51LDJ station are greater than those in the EW and UD components. Moreover, as the period exceeds 1.0 s, the acceleration response spectra in the NS component exhibit faster attenuation compared to the EW and UD components. However, for stations 51LDL and 51SMM, the acceleration response spectra of all three components exhibit similar decay rates when the period exceeds 1.0 s.

### 2.3 Spatial distribution of horizontal ground motion

In this study, horizontal ground motion is defined as the orientation-independent ROTD50 of ground motion in the EW and NS components (Boore 2010). Figure 3 presents the spatial distribution of observed horizontal PGA, PGV, and the spectral acceleration for periods of 0.1, 0.5, 1.0, and 3.0 s. The largest recorded horizontal PGA is 335.224 gal at station 51SMM, followed by the second largest horizontal PGA of 241.98 gal at station 51LDL. Additionally, the largest horizontal PGV is 20.714 cm/s recorded at station 51LDJ. It should be noted that none of these three stations are located on the fault rupture plane. Among the

**Table 2** Ground motion and site parameters for recording stations with rupture distances less than 50 km observed in the  $M_w$  6.6 Luding earthquake

| Station Name | Longitude (°) | Latitude (°) | NEHRP site classification | $V_{S30}$ (m/s) | Rupture distance(km) | PGA (gal) |        |        | PGV (cm/s) |       |      |
|--------------|---------------|--------------|---------------------------|-----------------|----------------------|-----------|--------|--------|------------|-------|------|
|              |               |              |                           |                 |                      | EW        | NS     | UD     | EW         | NS    | UD   |
| 51LDJ        | 102.2         | 29.7         | D                         | 306.14          | 12.87                | 118.87    | -      | 160.00 | -          | 37.59 | -    |
|              |               |              |                           |                 |                      |           | 316.00 |        | 12.83      |       | 7.74 |
| 51SMX        | 102.3         | 29.3         | D                         | 313.79          | 15.17                | 179.10    | 176.47 | 157.70 | -          | -     | 8.85 |
|              |               |              |                           |                 |                      |           |        |        | 11.60      | 10.35 |      |
| SCTS         | 102.3         | 29.3         | C                         | 421.34          | 15.18                | 179.56    | 187.01 | 171.09 | 11.32      | 13.08 | 9.25 |
| 51LDL        | 102.2         | 29.8         | D                         | 310.06          | 18.95                | 301.98    | -      | -      | 12.48      | -     | -    |
|              |               |              |                           |                 |                      |           | 193.75 | 203.09 |            | 12.05 | 6.06 |
| SCVL         | 102.2         | 29.9         | C                         | 503.78          | 27.17                | 91.85     | 166.81 | 136.76 | 5.11       | -4.24 | 3.02 |
| 51SMM        | 102.4         | 29.3         | D                         | 295.62          | 27.27                | -         | -      | 114.21 | -          | 9.31  | 4.57 |
|              |               |              |                           |                 |                      |           |        |        | 12.53      |       |      |
| 51LDS        | 102.2         | 29.9         | D                         | 345.30          | 29.82                | 61.21     | 46.07  | 87.85  | 3.97       | -2.75 | -    |
|              |               |              |                           |                 |                      |           |        |        |            |       | 2.27 |
| 51SMC        | 102.3         | 29.1         | D                         | 313.33          | 32.08                | 87.89     | 78.79  | 43.51  | 5.57       | -6.33 | 2.03 |
| SCSM         | 102.5         | 29.3         | C                         | 381.53          | 32.38                | 97.31     | 165.86 | 5.97   | -5.10      | -9.25 | 0.36 |
| SCHY         | 102.5         | 29.6         | C                         | 429.06          | 36.79                | 34.68     | 45.94  | 19.68  | 4.26       | -8.81 | -    |
|              |               |              |                           |                 |                      |           |        |        |            |       | 2.17 |
| SCTT         | 102.4         | 29.9         | C                         | 579.44          | 39.72                | 111.27    | 83.86  | 55.09  | -2.32      | 3.33  | 1.88 |
| SCTH         | 102.6         | 29.5         | D                         | 240.92          | 42.78                | 58.81     | 63.18  | 39.02  | -6.33      | -7.37 | -    |
|              |               |              |                           |                 |                      |           |        |        |            |       | 4.00 |
| SCTY         | 102.5         | 29.8         | C                         | 391.69          | 43.24                | 184.20    | 127.08 | 29.21  | -6.48      | -6.34 | -    |
|              |               |              |                           |                 |                      |           |        |        |            |       | 1.60 |
| 51HYQ        | 102.6         | 29.6         | D                         | 328.53          | 47.34                | 50.14     | 76.94  | 26.88  | -5.72      | 7.01  | 2.74 |
| SCVK         | 101.6         | 29.8         | C                         | 401.84          | 47.88                | 53.49     | 71.88  | 47.19  | -1.73      | -2.52 | 1.31 |

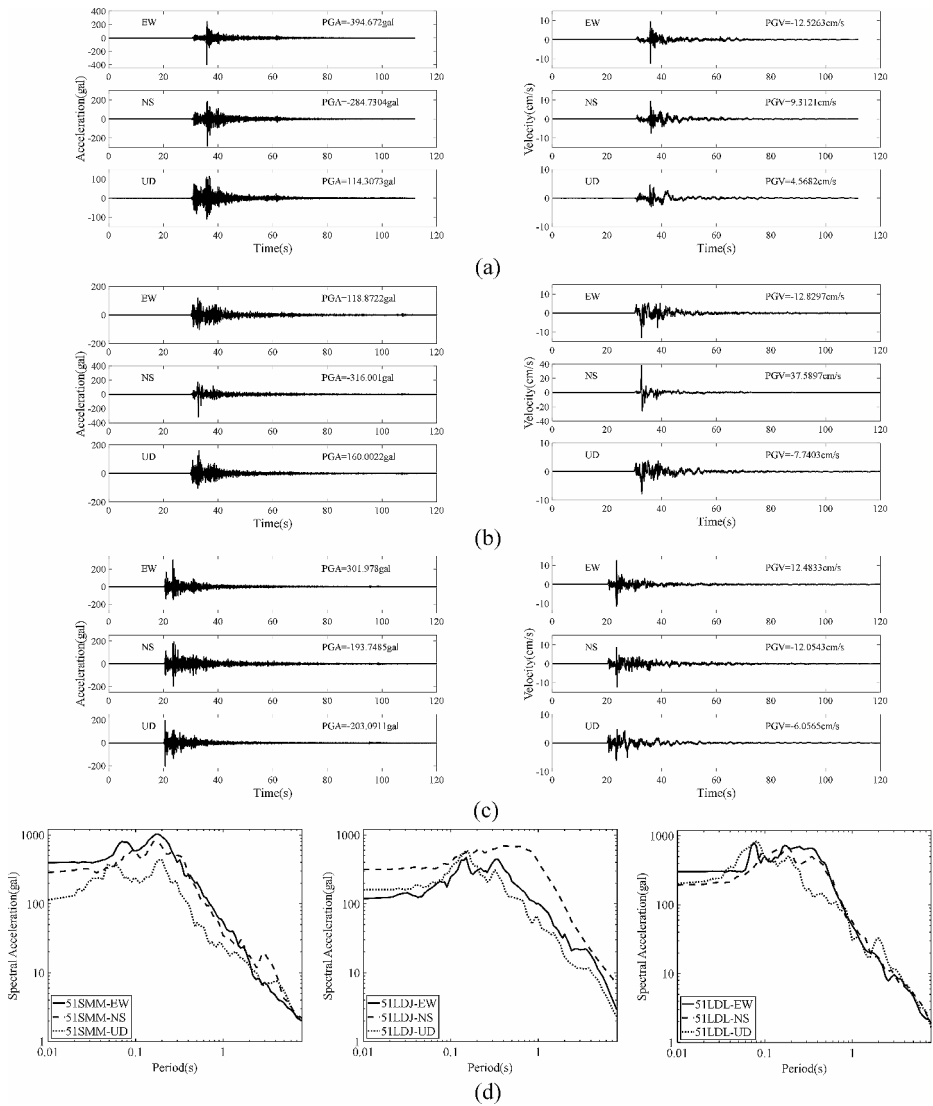


**Fig. 2** (a–c) Acceleration, velocity time histories, and (d) acceleration response spectra in the EW, NS, and UD components of 51SMM, 51LDJ, and 51LDL stations

15 near-fault stations with  $R_{rup}$  less than 50 km, the horizontal PGAs range from 39.91 gal to 335.22 gal, while the horizontal PGVs range from 2.09 cm/s to 20.71 cm/s.

By conducting a survey of earthquake damage in the disaster area and utilizing scientific and technological achievements such as instrument intensity, aftershock distribution, seismic structure background, focal mechanism, and remote sensing images, the China Earthquake Administration (CEA) has compiled the Modified Mercalli Intensity (MMI) Map for the  $M_W$  6.6 Luding earthquake ([https://www.mem.gov.cn/xw/yjglbgzdt/202209/t20220911\\_422190.shtml](https://www.mem.gov.cn/xw/yjglbgzdt/202209/t20220911_422190.shtml)). According to the published MMI map, the maximum MMI is



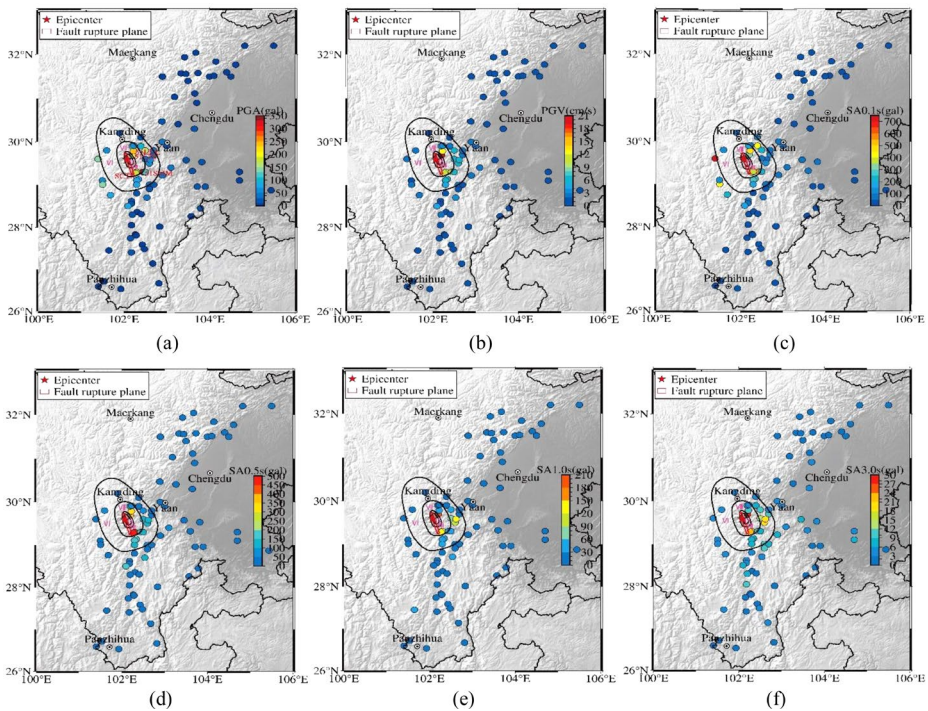


**Fig. 3** Spatial distribution of observed horizontal (a) PGA, (b) PGV, and spectral accelerations at periods (c) 0.1 s, (d) 0.5 s, (e) 1.0 s, and (f) 3.0 s. Red star indicates the epicenter. Red rectangle denotes the fault rupture plane of the  $M_w$ 6.6 Luding earthquake (Zhang et al. 2023). Black circle line indicates the published MMI. The observed stations are shown in circles, and the PGA, PGV, and spectral accelerations are shown in the color scale

**Table 3** PGA interval values corresponding to Chinese seismic intensity

| Chinese seismic intensity | <VI   | VI        | VII        | VIII        | IX          | X    |
|---------------------------|-------|-----------|------------|-------------|-------------|------|
| PGA (gal)                 | <45.7 | 45.7–93.6 | 93.7–194.0 | 195.0–401.0 | 402.0–830.0 | ≥831 |
| EW                        | 66    | 9         | 9          | 2           | 0           | 0    |
| NS                        | 62    | 11        | 9          | 2           | 0           | 0    |
| UD                        | 76    | 3         | 6          | 1           | 0           | 0    |

IX, as indicated by the black circle line in Fig. 3. The stations exhibiting PGA greater than 100 gal and PGV exceeding 3 cm/s are predominantly situated within the region where the published MMI is equal to or larger than VI. It is worth noting that both PGA and PGV values decrease rapidly with rupture distances increase. Figure 3 shows that the spatial distribution of horizontal PGA, PGV, and spectra acceleration with periods of 0.1, 0.5, 1.0, and 3.0 s aligns with the published MMI distribution. Tables 3 and 4 provide the PGA and PGV interval values corresponding to the Chinese seismic intensity (hereafter CSI, State Administration for Market Regulation and China National Standardization Administration Committee 2020). The CSIs corresponding to the horizontal PGAs and PGVs recorded at stations 51SMM and 51LDL are VIII and VII, respectively. However, these two stations are located in the area where the published MMI is VII. Despite being located in an area with a

**Table 4** PGV interval values corresponding to Chinese seismic intensity

| Chinese seismic intensity | <VI   | VI        | VII       | VIII      | IX        | X     |
|---------------------------|-------|-----------|-----------|-----------|-----------|-------|
| PGV (cm/s)                | <3.81 | 3.81–8.17 | 8.18–17.6 | 17.7–37.8 | 37.9–81.4 | >81.4 |
| EW                        | 70    | 11        | 5         | 0         | 0         | 0     |
| NS                        | 71    | 8         | 6         | 1         | 0         | 0     |
| UD                        | 80    | 4         | 2         | 0         | 0         | 0     |

published MMI less than VI, the stations 51JLT and 51MNT, which are situated at rupture distances of 85.56 km and 120.78 km, exhibit recorded PGA and PGV values of 139.66 gal and 2.28 cm/s, and 87.10 gal and 4.25 cm/s, respectively. Interestingly, the corresponding CSIs for the PGAs recorded at these two stations are VII and <VI, while the CSIs for PGVs are VI and VI, respectively. This suggests that the CSIs aligned with the recorded PGV values demonstrate a greater consistency with the published MMI. According to the investigations of the strong-motion station construction report, it is revealed that all four stations are located on gentle slopes or half slopes in front of the mountain. These locations are classified as NEHRP site class C or D sites. It is believed that the recorded PGA values at these stations may undergo amplification due to the influence of terrain or small basin effects.

At period  $T=0.1$  s, the maximum horizontal spectral acceleration is 702.86 gal for the base station SCVK. The stations with spectral accelerations greater than 500 gal are SCVK and 51SMM. Furthermore, it is observed that the majority of stations with spectral accelerations greater than 100 gal are located within an area where the published MMI is equal to or greater than VI. Moreover, these spectral accelerations tend to attenuate rapidly as the rupture distance increases. At period  $T=0.5$  s, all horizontal spectral accelerations are less than 500 gal, and the maximum horizontal spectral acceleration is 466.02 gal at the basic station SCTS. With the exception of station 51MNT, the stations exhibiting spectral accelerations greater than 100 gal are located within areas where the published MMI is equal to or greater than VI. At period  $T=1.0$  s, station 51LDJ recorded the maximum spectral acceleration of 205.08 gal, while only 5 stations exhibited spectral accelerations greater than 100 gal. At period  $T=3.0$  s, all the spectral accelerations are less than 30 gal, with the maximum spectral acceleration being 27.06 gal at station 51LDJ.

## 2.4 Rupture directivity effect

The rupture directivity effect of a seismic fault can significantly influence ground motion. The recent generation of seismic hazard map in the United States has begun to take into account the impacts of rupture directivity effect (Petersen et al. 2014; Field et al. 2014).

### 2.4.1 Spatial distribution of the residual

To compare the difference in ground motion between sites in the rupture forward and backward directions, it is necessary to eliminate the average effect of ground motion attenuation. This can be achieved by calculating the residuals from the ground motion attenuation relationship. In our study, we developed a specific ground motion attenuation relationship by utilizing strong motion data from the  $M_w$  6.6 Luding earthquake. We employed the residuals obtained from this relationship to assess the systematic differences in ground motion between the rupture forward and backward directions. To accomplish this, we adopted the



functional form of the simplified ground motion attenuation model, as shown in Eq. 1. All observed data are adjusted to site condition of  $V_{S30}=760$  m/s based on the Seyhan and Stewart (2014) model.

$$\ln Y = a_0 + a_1 \ln (R_{rup} + a_2) + a_3 R_{rup} \quad (1)$$

where  $Y$  is the ground motion parameters PGA, PGV, SA ( $T=0.1, 0.5, 1.0, 3.0, 5.0, 7.5$  and  $10.0$  s). The coefficients  $a_0, a_1, a_2$ , and  $a_3$  are obtained by least-squares fitting.  $a_1$  and  $a_3$  represent the coefficients of geometric and anelastic attenuation, respectively. The residuals were calculated by Eq. 2.

$$R_{es} = \ln (Y_{obs}) - \ln (Y_{pre}) \quad (2)$$

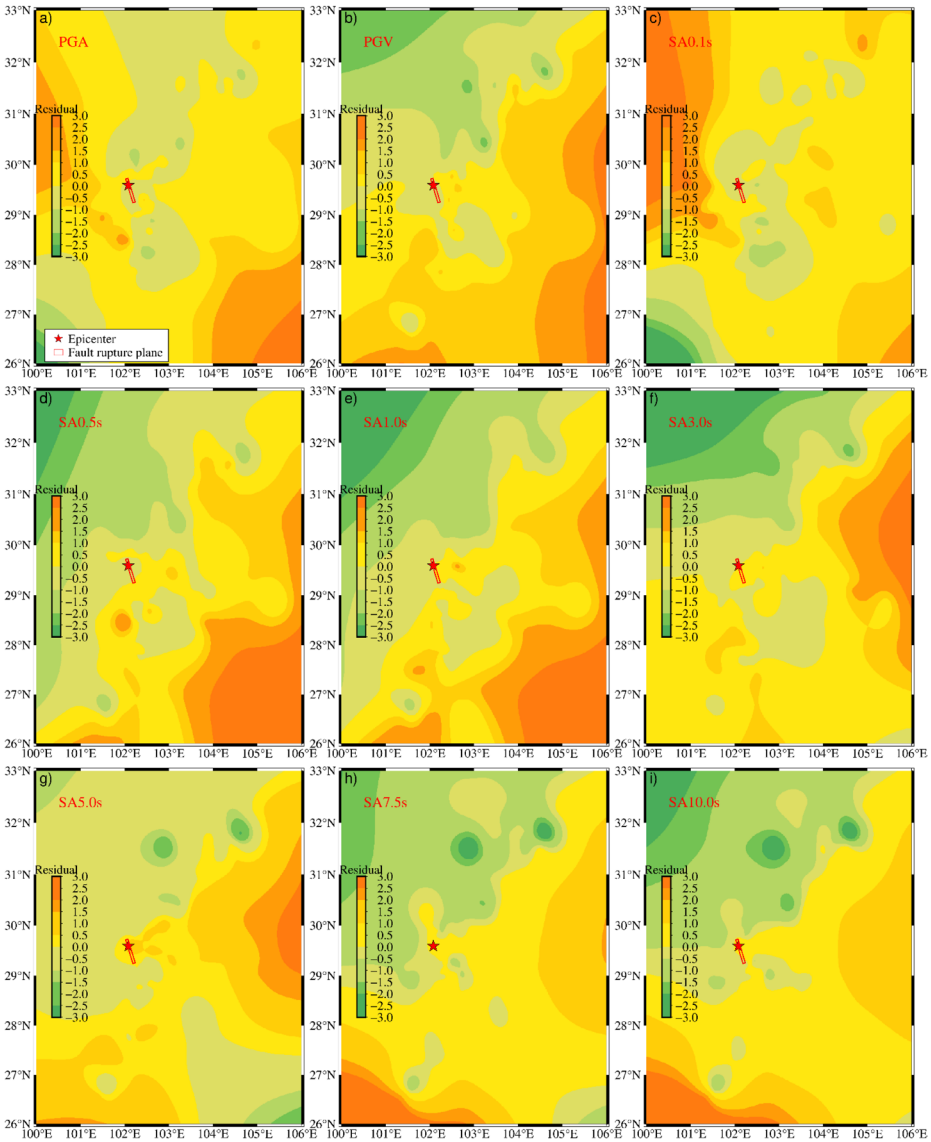
where  $R_{es}$  is the residual,  $Y_{obs}$  is the observed ground motion, and  $Y_{pre}$  is the predicted ground motion.

Figure 4 shows the spatial distribution of the residuals for horizontal PGA, PGV, and SA ( $T=0.1, 0.5, 1.0, 3.0, 5.0, 7.5$  and  $10.0$  s) obtained from the simplified attenuation model. The fault rupture process predominantly occurs from the epicenter towards the south-south-east direction of the seismogenic fault, exhibiting distinct unilateral rupture characteristics (Zhang et al. 2023). Figure 4 reveals that there is a minimal disparity between the residuals of PGA and PGV in the rupture forward and backward directions. However, a notable trend emerges for SA ( $T=0.1, 0.5, 1.0, 3.0, 5.0, 7.5$  and  $10.0$  s). In the rupture forward direction, the majority of residuals for SA ( $T=0.1, 0.5, 1.0, 3.0, 5.0, 7.5$  and  $10.0$  s) are positive, indicating that the observed ground motions are greater than the predicted values. Conversely, in the rupture backward direction, most residuals for SA ( $T=0.1, 0.5, 1.0, 3.0, 5.0, 7.5$  and  $10.0$  s) are negative, suggesting that the observed ground motions are lower than the predicted values. For periods exceeding  $3.0$  s, the difference between the residuals in the rupture forward and backward directions gradually decreases with increasing period. This suggests that the ground motion of the strike-slip  $M_W$  6.6 Luding earthquake exhibits a notable directivity effect across various periods, especially in medium periods. Specifically, the ground motion parameters recorded in the rupture forward direction are greater than the average level, while those in the rupture backward direction are fall below the average level.

## 2.4.2 Quantitative analysis of near-fault directivity effect

Based on the analysis of strong motion observation, Xie et al. (2017) have identified a significant insufficient in the directivity effect model proposed by Bayless and Somerville (2013) in the NGA-West2 project. Specifically, this model fails to accurately estimate the attenuation effect of long-period ground motion in the rupture backward direction. In their study, Xie et al. (2017) revised the directivity model of Bayless and Somerville (2013) and introduced a new quantitative prediction model for directivity effects based on the observation results. This improved model allows for a quantitative analysis of both the amplification effect in the rupture forward direction and the attenuation effect in the rupture backward direction. The parameter model for quantitative prediction of directivity effect is as follows.

$$f_g = \ln S \cdot \cos(\theta), \quad 0 \leq \theta < 180^\circ \quad (3)$$



**Fig. 4** Spatial distribution of residuals for horizontal (a) PGA, (b) PGV, and (c-l) SA ( $T=0.1, 0.5, 1.0, 3.0, 5.0, 7.5$  and  $10.0$  s) obtained from the simplified attenuation model

in which,  $S$  represents the length of the rupture surface projected along the strike towards the site (in km).  $\theta$  ( $^\circ$ ) denotes the angle between the direction of the rupture and the direction from the source to the site. In the directivity model proposed by Xie et al. (2017), the cosine value was directly used to express the influence of  $\theta$ ,  $0^\circ < \theta < 90^\circ$  represents the position of influence in the rupture forward direction, while  $90^\circ < \theta < 180^\circ$  represents the position of influence in the rupture backward direction. It is worth noting that in line with NGA-West2

guidelines, the parameter  $f_g$  is taken as a dimensionless scalar in the study, representing solely the strength of the directivity effect.

To quantitative analysis of the rupture directivity effect on  $S$  and  $\theta$ , we utilized strong motion data from 37 stations with rupture distances less than 100 km. In Fig. S1, we present the variation of regression residuals as a function of  $\cos(\theta)$ . Our findings indicate that there is no significant systematic deviation in the regression residuals of PGA and PGV with the change of  $\cos(\theta)$ . However, the regression residuals of spectral acceleration at periods greater than 0.1 s exhibit a linear increase with the change of  $\cos(\theta)$ . In the rupture forward (when  $\cos(\theta)$  is positive), the residual values of most observation points are positive, indicating that the observed ground motions are generally greater than the average value. Conversely, in the rupture backward direction (when  $\cos(\theta)$  is negative), the residual values of most observation points are negative, indicating that the observed ground motions are typically less than the average value.

In Fig. S2, we present the variation of regression residuals for PGA, PGV, and  $Sa$  ( $T=0.1, 0.5, 1.0, 3.0, 5.0, 7.5,$  and  $10.0$  s) with  $\ln(S)$ . Our analysis reveals that the regression residuals of PGA and PGV do not exhibit significant systematic deviation with  $\ln(S)$ . However, the regression residuals of spectral acceleration at periods greater than 0.1 s show an increase as the rupture length increases. These findings suggest that the amplification effect in the rupture forward direction and the attenuation effect in the rupture backward direction gradually intensify with a longer rupture length.

Based on the observed trends in the variation of regression residuals with azimuth angle  $\theta$  and rupture length  $S$ , it is speculated that a strong linear relationship exists between the residuals and the predictor parameter of directivity effect  $f_g$ . To explore this relationship, the log-linear model proposed by Bayless and Somerville (2013) can be employed to fit the regression residuals with  $f_g$ . The equation representing this linear fit is referred to as Eq. 4 in the study.

$$f_D = C_0 + C_1 \cdot f_g \tag{4}$$

$f_D$  is the regression residual in log, and  $C_0$  and  $C_1$  are the fitting coefficients.

In Fig. 5, the changes in regression residuals of PGA, PGV, and  $Sa$  ( $T=0.1, 0.5, 1.0, 3.0, 5.0, 7.5,$  and  $10.0$  s) with  $f_g$  are depicted, along with the linear fitting line for the residuals. Additionally, Table 5 presents the primary parameters of the directivity effect model for PGA, PGV, and  $Sa$  ( $T=0.1, 0.5, 1.0, 3.0, 5.0, 7.5,$  and  $10.0$  s). Furthermore, Table 6 displays the influence coefficients of directivity effects on ground motion at various periods in both the rupture forward ( $\theta=0^\circ, f_g=4.0$ ) and rupture backward ( $\theta=180^\circ, f_g=-4.0$ ) directions, as per the model results obtained through statistical regression analysis of directivity effects. The results indicate that in the rupture forward direction, the spectral accelerations at periods of 0.1, 0.5, 1.0, 3.0, 5.0, 7.5, and 10.0 s are amplified to 0.2475, 0.2012, 0.3057, 0.1494, 0.1726, 0.0962, and 0.0798 times the observed mean, respectively. Conversely, in the rupture backward direction, the spectral accelerations at periods of 0.1, 0.5, 1.0, 3.0, 5.0, 7.5, and 10.0 s are weakened to 0.2831, 0.2407, 0.1828, 0.0738, 0.1354, 0.0855, and 0.0747 times the observed mean, respectively. The effect of rupture directivity is most pronounced in amplifying the spectral acceleration at a period of 1.0 s in the rupture forward direction and in weakening the spectral acceleration at a period of 0.5 s in the rupture backward direction.

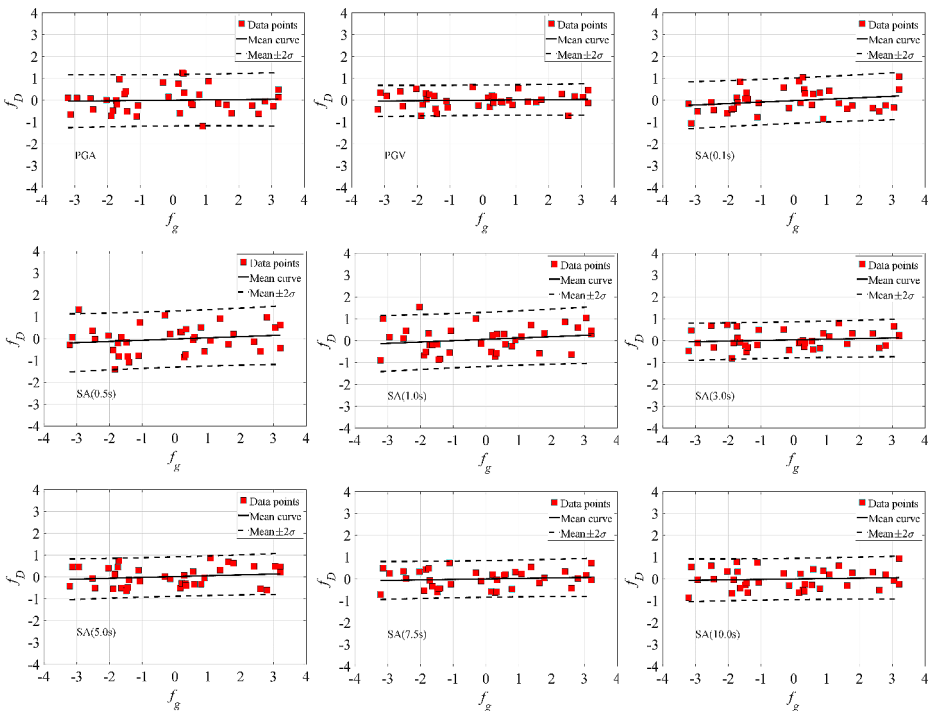


**Fig. 5** Variation of residuals with geometric directivity predictor parameter  $f_g$  for PGA, PGV, and SA ( $T=0.1, 0.5, 1.0, 3.0, 5.0, 7.5,$  and  $10.0$  s)

**Table 5** Summary of regression results for directivity effects based on the proposed log-linear model

| Observed ground motion parameters | $C_1$  | $C_0$   | RMSD   |
|-----------------------------------|--------|---------|--------|
| PGA                               | 0.0133 | 0.0025  | 0.5950 |
| PGV                               | 0.0111 | 0.0025  | 0.3509 |
| Sa (0.1s)                         | 0.0663 | -0.0178 | 0.5258 |
| Sa (0.5s)                         | 0.0552 | -0.0197 | 0.6504 |
| Sa (1.0s)                         | 0.0611 | 0.0615  | 0.6278 |
| Sa (3.0s)                         | 0.0279 | 0.0378  | 0.4183 |
| Sa (5.0s)                         | 0.0385 | 0.0186  | 0.4560 |
| Sa (7.5s)                         | 0.0227 | 0.0054  | 0.4245 |
| Sa (10.0s)                        | 0.0193 | 0.0025  | 0.4790 |

**Table 6** The amplification and de-amplification coefficients of directivity effects on spectral accelerations at different periods

| Amplification              | SA      |         |         |         |         |         |         |  |
|----------------------------|---------|---------|---------|---------|---------|---------|---------|--|
|                            | 0.1 s   | 0.5 s   | 1.0 s   | 3.0 s   | 5.0 s   | 7.5 s   | 10.0 s  |  |
| Rupture forward direction  | 0.2475  | 0.2012  | 0.3057  | 0.1494  | 0.1726  | 0.0962  | 0.0798  |  |
| Rupture backward direction | -0.2831 | -0.2407 | -0.1828 | -0.0738 | -0.1354 | -0.0855 | -0.0747 |  |

## 2.5 Near-fault velocity pulses

The wavelet method (Baker 2007) was used to identify the velocity pulses characteristics of the near-fault strong motion recordings of this earthquake. To consider the uncertainty in the direction of the velocity pulses, the observed ground motion was rotated in the horizontal plane (Shahi and Baker 2011). This allowed for the identification of velocity pulses in all horizontal directions and the classification of a recording as pulse-like when it exhibited typical velocity pulse characteristics. Through the analysis of ground motion recordings from the Luding earthquake, a distinct pulse-like recording was identified at the 51LDJ station, located at a rupture distance of 12.87 km. The orientation of the pulse-like recording is shown in Fig. 6a, with the maximum pulse direction being N6°E. This earthquake is classified as a typical strike-slip earthquake, and the maximum pulse recorded by the 51LDJ station aligns with the vertical fault direction, as indicated by the black arrow in Fig. 1. This alignment is consistent with the pulse characteristics observed in common strike-slip earthquakes (Baker 2007; Xie et al. 2012). Figure 6b shows the waveform of pulse-like recording along the maximum pulse direction, revealing the presence of typical bidirectional pulse characteristics and PGV of 37.0 cm/s.

## 3 Comparison with the new GMPE in Southwest China

### 3.1 Comparison of horizontal ground motion with new GMPE in Southwest China

Zhang et al. (2022) developed a horizontal GMPE (ZYLW22) based on the 1324 ROTD50 data of 70 mainshocks with magnitudes  $4.2 \leq M_W \leq 7.9$  that occurred in southwest China from 2008 to 2018. The ZYLW22 GMPE is suitable for rupture distances of up to 200 km. The observed horizontal ground motion parameters, including PGA, PGV, and SA ( $T=0.1, 0.5, 1.0, \text{ and } 3.0 \text{ s}$ ) of the  $M_W$  6.6 Luding earthquake, were compared to the median predictions of the ZYLW22 GMPE, as shown in Fig. 7. The black dashed line represents  $\pm 1$  times the standard deviation of the median prediction. It is observed that a majority of the horizontal ground motion parameters within 200 km of the  $M_W$  6.6 Luding earthquake

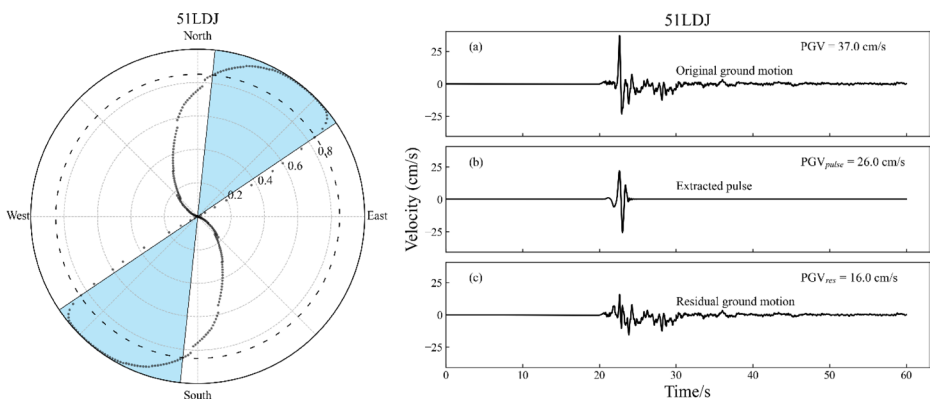


**Fig. 6** Occurrence of azimuth (a) and velocity wave forms (b) of typical pulse-like recording in station 51LDJ

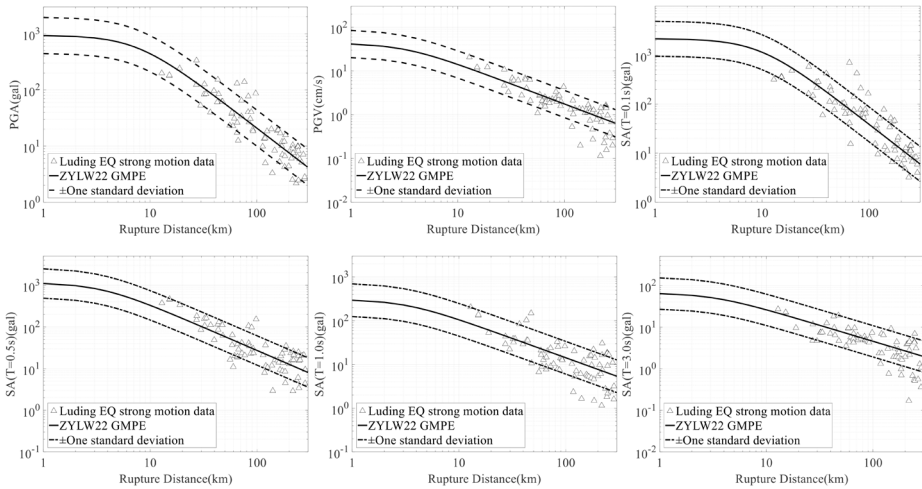


**Fig. 7** Comparison of observed horizontal ground motions with the median predictions obtained from the ZYLW22 GMPE

fall within  $\pm 1$  times standard deviation curve of the median predictions obtained from the ZYLW22 GMPE. This suggests that the ZYLW22 GMPE can effectively predict most of the horizontal ground motion of the  $M_W$  6.6 Luding earthquake. However, the short-period ground motions (PGA, SA ( $T=0.1$  and  $0.5s$ )) recorded at SCVK, 51JLT, 51JLN, and 51MNT stations, all located with rupture distances of less than 100 km, are slightly higher than  $+1$  times the standard deviation of the median predictions. According to the survey of the station construction reports, these four stations are located on the second-class terrace or gentle slope of the piedmont on both sides of the river valley, with slopes ranging from  $40^\circ$  to  $50^\circ$ . In contrast, most other station sites are flat and open. The heightened short-period ground motions observed at these specific stations could potentially be influenced by topographic amplification effects.

### 3.2 Residual analysis

On 20 April 2013, a  $M_W$  6.7 earthquake occurred in Lushan County, Sichuan Province. The CENC reported the earthquake’s epicenter at  $30.30^\circ N$ ,  $103.00^\circ E$ , with a focal depth of 13 km. Wang et al. (2013) conducted a rapid inversion using far-field body wave data and the finite fault method to obtain a focal rupture process model. The results indicated that the earthquake was a thrust fault earthquake at the southern end of the Longmenshan fault zone. The maximum published MMI of this event was IX. On 8 August 2017, a  $M_W$  6.5 earthquake occurred in Jiuzhaigou County, Sichuan Province. The earthquake’s epicenter was  $33.20^\circ N$ ,  $103.82^\circ E$ , with a focal depth of 20 km. Zhang et al. (2017) utilized inversion results from far-field body wave data and near-field co-seismic InSAR data to determine that this earthquake was a left-lateral strike-slip event. It was presumed to have taken place along the northward extension of the Huya fault. The maximum MMI during this earthquake reached IX.



Residual analysis of strong motion data is an effective tool to identify the impact of seismic sources and propagation paths on ground motion. It can also identify the primary factors influencing regional differences in ground motion (Rodriguez-Marek et al. 2011; Wen et al. 2018; Xu et al. 2020). The total residual ( $R_{es}$ ) is determined by calculating the difference between the observed value and the predicted value at each station. This total residual can be further divided into inter-event residual ( $\eta_e$ ) and intra-event residual ( $\varepsilon_{es}$ ) (Al Atik et al. 2010), as shown in Eq. 5.

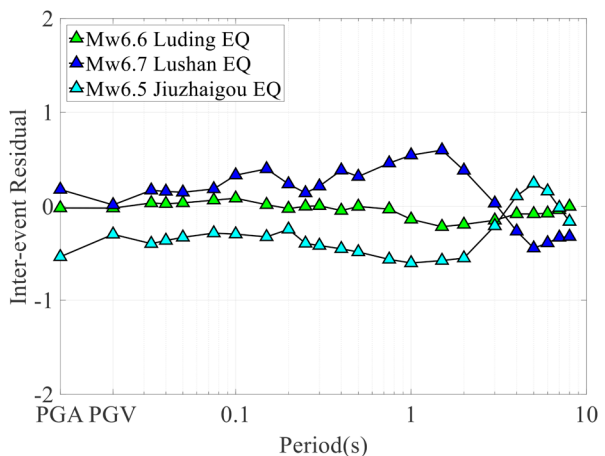
$$R_{es} = \eta_e + \varepsilon_{es} \tag{5}$$

In which the subscripts  $e$  and  $s$  denote earthquake and station, respectively.

The inter-event residual  $\eta_e$  represents the mean deviation of earthquake-related observations and median predictions obtained from the GMPE. Source effect encompasses the influence of rock mass properties in the source area, the energy release characteristics and radiation during the source rupture process, and the average stress drop resulting from rock mass fracture on the ground motion caused by an earthquake. As such, variations in inter-event residual  $\eta_e$  can be used to represent the difference in source effect. Variations in crustal structure, such as the quality factor  $Q$ , can induce alterations in anelastic attenuation over longer distances, thereby significantly influencing ground motions beyond 80 km (Abrahamson et al. 2014; Boore et al. 2014). For a particular earthquake, the inter-event residual is calculated by averaging the residuals between the observed values and the median predictions obtained from the GMPE at  $R_{rup} < 80$  km (Xu et al. 2020). Figure 8 shows the distribution of inter-event residuals at rupture distances of 0–200 km for the 2013  $M_w$  6.7 Lushan earthquake, the 2017  $M_w$  6.5 Jiuzhaigou earthquake, and the 2022  $M_w$  6.6 Luding earthquake. The epicenters of these three earthquakes are shown in Fig. 1.

For the  $M_w$  6.6 Luding earthquake, the inter-event residuals over the entire period are negative, with slightly negative inter-event residuals for SA ( $T < 0.5$  s). For the  $M_w$  6.5 Jiuzhaigou earthquake, the inter-event residuals are negative for SA ( $T < 3.0$  s) and SA ( $T \geq 6.0$  s), while being positive for SA ( $3.0 \text{ s} \leq T < 6.0 \text{ s}$ ). For the  $M_w$  6.7 Lushan earthquake, the inter-event residuals are positive for SA ( $T < 3.0$  s), while being negative for SA ( $T > 3.0$  s). Comparing to the Jiuzhaigou earthquake, the inter-event residuals for PGA,

**Fig. 8** Inter-event residuals of PGA, PGV, and SAs at periods up to 8.0 s for the  $M_w$ 6.6 Luding,  $M_w$ 6.7 Lushan, and  $M_w$ 6.5 Jiuzhaigou earthquakes based on the ZYLW22 GMPE



PGV, SA ( $T < 3.0$  s), and SA ( $T > 7.0$  s) are larger in the Luding earthquake. However, the inter-event residuals for SA ( $3.0 < T < 7.0$  s) are larger in the Jiuzhaigou earthquake than in the Luding earthquake. These results indicate that the source effect of the strike-slip Luding and Jiuzhaigou earthquakes is weaker when compared to the average level of shallow crustal mainshocks in southwest China as considered in the ZYLW22 GMPE. Specifically, for periods less than 3.0 s, the source effect of the Luding earthquake is stronger than that of the Jiuzhaigou earthquake. On the other hand, the source effect of the thrust-fault Lushan earthquake is stronger than the average level of shallow crustal mainshocks in southwest China in short and medium periods, but weaker than the average level of shallow crustal mainshocks in long periods.

Figure 9 shows the distribution of the intra-event residuals for PGA, PGV, and SA ( $T = 0.1, 0.5, 1.0,$  and  $3.0$  s) as a function of rupture distance for the Luding, Lushan, and Jiuzhaigou earthquakes, as calculated based on the ZYLW22 GMPE. The intra-event residuals of ground motion for the Luding earthquake show a decrease in each period, correlating with the rupture distance. However, the amplitude of this decrease is minimal. On the other hand, the intra-event residuals of short-period ground motion (PGA, SA ( $T = 0.1$  and  $0.5$  s) for the Lushan earthquake exhibit an increase with rupture distance increases. Conversely, the intra-event residuals of medium- and long-period ground motion (PGV, SA ( $T = 1.0$  and  $3.0$ s) remain unchanged with rupture distance. The intra-event residuals of the short-period ground motion (PGA, SA ( $T = 0.1$  s) for the Jiuzhaigou earthquake show a decrease with rupture distance, while the intra-event residuals of the medium- and long-period ground motion (PGV, SA ( $T = 1.0$  and  $3.0$  s) reveal a slight increase with rupture distance. These results indicate that the ZYLW22 GMPE effectively captures the anelastic attenuation characteristics in the three strong earthquake areas of Sichuan Province, especially in medium and long periods. This contrasts with the Boore et al. (2013) GMPE, which indicated lower anelastic attenuation due to a higher crustal quality factor  $Q$  in the Lushan earthquake area, as highlighted by Wen and Ren (2014). The anelastic attenuation ( $Q$ ) in the Longmenshan, Xianshuihe, and Huya fault zones exhibits significant regional variability and periodic cor-

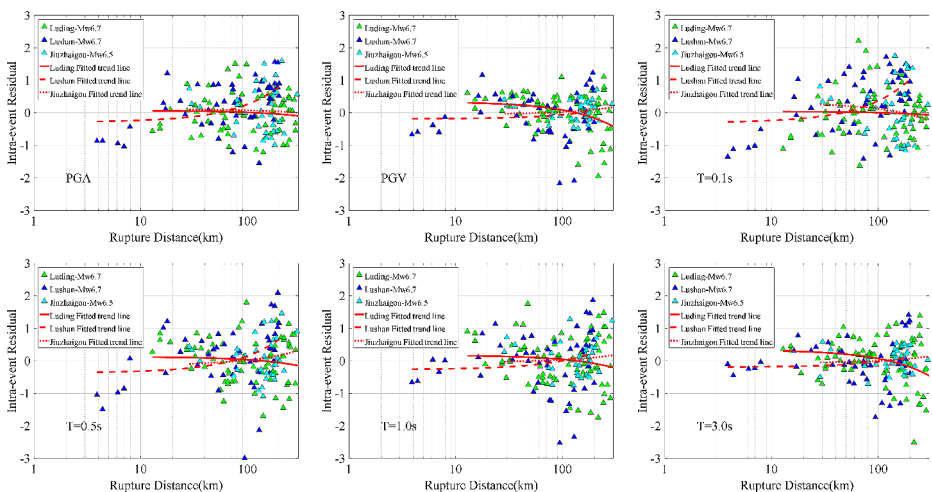


**Fig. 9** Intra-event residuals of PGA, PGV, and SA ( $T = 0.1, 0.5, 1.0,$  and  $3.0$  s) for the  $M_W 6.6$  Luding,  $M_W 6.7$  Lushan, and  $M_W 6.5$  Jiuzhaigou earthquakes based on the ZYLW22 GMPE

relation, which can be attributed to variations in the regional tectonic background and the heterogeneity of crustal structure. This observation aligns with the findings reported by Graizer (2022).

## 4 Summary and conclusions

In this study, we preliminarily analyzed the near-fault ground motion amplitude, acceleration response spectra characteristics, and the spatial distribution of horizontal ground motions for the  $M_W$  6.6 Luding earthquake. The residuals obtained from the simplified ground motion attenuation model were utilized to evaluate and quantify the difference in horizontal ground motion between the rupture forward and backward directions. Then the pulse-like feature of near-fault ground motion was investigated. Based on the ZYLW22 GMPE in southwest China, we investigated whether the  $M_W$  6.6 Luding earthquake conforms to the observed ground motion attenuation characteristics in the mainshocks of this region. Additionally, the factors that influence the variation in ground motion for three earthquakes with similar magnitude in Sichuan Province were investigated.

The results indicate that most of the larger PGA, PGV, and spectral accelerations at each period are located in areas where the published MMI is equal to or greater than VI. Furthermore, the horizontal ground motion exhibits rapid attenuation with increasing rupture distance. The CSIs corresponding to the recorded PGAs and PGVs are consistent with the distribution of published MMI, especially for the CSIs corresponding to the recorded PGVs. The analysis reveals that the Luding earthquake exhibits the strongest horizontal ground motion at the short period  $T=0.1$  s, with a maximum spectral acceleration is 702.86 gal. However, for the long periods ( $T=3.0$  s), all spectral accelerations are below 30 gal.

The spatial distribution of the residual reveals a minimal disparity between the residuals of PGA and PGV in the rupture forward and backward directions. However, a notable trend emerges for SA ( $T=0.1, 0.5, 1.0, 3.0, 5.0, 7.5$  and  $10.0$  s). In the rupture forward direction, the observed ground motions are greater than the predicted values. Conversely, in the rupture backward direction, the observed ground motions are lower than the predicted values. The ground motion of the strike-slip  $M_W$  6.6 Luding earthquake exhibits a notable directivity effect across various periods, especially in medium periods.

The quantitative analysis of the rupture directivity effect on rupture length  $S$  and azimuth angle  $\theta$  indicates that there is no significant systematic deviation in the regression residuals of PGA and PGV with the change of  $\cos(\theta)$  and  $\ln(S)$ . However, the regression residuals of spectral acceleration at periods greater than 0.1 s exhibit a linear increase with the change of  $\cos(\theta)$  and  $\ln(S)$ . The linear model between the residuals and the directivity effect parameter  $f_g$  indicates that in the rupture forward direction, the spectral accelerations at periods 0.1–10.0 s are amplified to 0.0798–0.305 times the mean level. Conversely, in the rupture backward direction, the spectral accelerations at periods 0.1–10.0 s are weakened to 0.0738–0.2831 times the mean level. The effect of rupture directivity is most pronounced in amplifying the spectral acceleration at a period of 1.0 s in the rupture forward direction, and in weakening the spectral acceleration at a period of 0.5 s in the rupture backward direction. From periods 1.0 s to 10.0 s, the influence of the rupture directivity effect typically diminishes with increasing period. This behavior markedly contrasts with the rupture directivity effect observed in 2016  $M_W$  7.0 Kumamoto earthquake in Japan (Xie et al. 2017), which is

primarily attributed to the imaging of two subevent in the slip distribution of the  $M_w$  6.6 Luding earthquake (Zhang et al. 2023). The directivity effect of near-fault ground motion for strike-slip earthquakes is primarily attributed to the directivity of the earthquake source rupture, often results in ground motion amplification in front of the fault rupture (Xie et al. 2017; An et al. 2019). The dominant rupture direction of this event is south-southeast (Zhang et al. 2023), aligning well with the findings drawn from our study. The maximum pulse direction recorded by the 51LDJ station is N6°E, aligning with the vertical fault direction. The velocity pulses had distinct bidirectional pulses in the waveforms, with a PGV of 37.0 cm/s.

The ZYLW22 GMPE exhibits the capability to effectively predict most of the horizontal ground motions observed in the Luding earthquake. The strong short-period ground motions observed at the four stations within 100 km may be attributed to the topographic amplification effect, such as steep slopes on both sides of the river valley or gentle slopes in the front of the mountain. The source effect of the strike-slip Luding and Jiuzhaigou earthquakes is weaker than the average level observed in shallow crustal mainshocks in southwest China. Furthermore, the source effect of the Luding earthquake on ground motion is stronger than that of the Jiuzhaigou event for periods less than 3.0 s. The thrust fault Lushan earthquake exhibits a source effect on ground motion that is stronger in short and medium periods but weaker in long periods, compared to the average level of shallow crustal mainshocks in southwest China. This observation aligns with the findings of Graizer (2018), who also noted higher amplitudes at short periods for thrust fault earthquakes. The ZYLW22 GMPE effectively capture the anelastic attenuation in the Sichuan strong earthquake area, especially in medium and long periods. The anelastic attenuation of the Longmenshan fault zone, Xianshuihe fault zone, and Huya fault zone in Sichuan exhibit significant regional variation and periodic correlation, which can be attributed to the variation in regional tectonic background and the heterogeneity of crustal structure.

The research findings indicate that the ground motion of strike-slip earthquakes in Sichuan exhibits a significant directivity effect in the medium and short periods. In addition, the source effect of three earthquakes with similar magnitude in Sichuan is closely linked to the fault type and period. To enhance the accuracy of ground motion predictions for seismic fortification, future GMPE construction in southwest China should comprehensively consider the directivity effect of strike-slip earthquakes in relation to periods. This is crucial as the original GMPE only considers the effects of fault type and would benefit from further integration of periodic correlations.

**Supplementary Information** The online version contains supplementary material available at <https://doi.org/10.1007/s10518-024-01934-9>.

**Acknowledgements** This work was supported by research grants from the National Key R&D Program of China (2022YFC3003503); the Major Program of National Natural Science Foundation of China (52192675); the 111 Project, China (D21001).

**Author contributions** Bin Zhang: Methodology, Writing–original draft, Visualization. Xiaojun Li: Conceptualization, Writing–review & editing. Yanxiang Yu: Formal analysis, Writing–review & editing. Xiaojian Lu: Data curation. Mianshui Rong: Writing–review & editing. Su Chen: Investigation. Zhao An: Software. Zhenghui Xiong: Validation.

**Data and Resources** Data for this study are provided by Engineering Mechanics, China Earthquake Administration.

## Declarations

**Competing interest** The authors declare that they have no known competing financial interests or personal relationships that could have appeared to influence the work reported in this study.

## References

- Abrahamson NA, Silva WJ, Kamai R (2014) Summary of the ASK14 ground motion relation for active crustal regions. *Earthq Spectra* 30(3):1025–1055. <https://doi.org/10.1193/070913eqs198m>
- Al Atik L, Abrahamson NA, Bommer JJ, Scherbaum F, Cotton F, Kuehn N (2010) The variability of ground-motion prediction models and its components. *Seismol Res Lett* 81(5):794–801. <https://doi.org/10.1785/gssrl.81.5.794>
- Allen TI, Wald DJ (2009) On the use of high-resolution topographic data as a proxy for seismic site conditions ( $V_s/30$ ). *Bull Seismol Soc Am* 99(2A):935–943. <https://doi.org/10.1785/0120080255>
- An Z, Xie JJ, Li XJ, Wen ZP (2019) Directivity effects on strong ground motion from the February 6, 2018  $M_W$  6.4 Hualian earthquake. *Chin J Geophys* 62(12):4658–4672. <https://doi.org/10.6038/cjg2019M0579> (in Chinese)
- Ancheta TD, Darragh RB, Stewart JP, Seyhan E, Silva WJ, Chiou BS-J, Wooddell KE, Graves RW, Kottke AR, Boore DM, Kishida T, Donahue JL (2013) PEER NGA-West2 database, PEER Report No. 2013/03. Pacific Earthquake Engineering Research Center, University of California, Berkeley, CA, p 134
- Baker JW (2007) Quantitative classification of near-fault ground motions using wavelet analysis. *Bull Seismol Soc Am* 97(5):1486–1501. <https://doi.org/10.1785/0120060255>
- Bayless J, Somerville P (2013) In: Spudich P (ed) Bayless-Somerville Directivity Model, Chap. 2 of PEER Report No. 2013/09. Pacific Earthquake Engineering Research Center, Berkeley, California
- Boore DM (2010) Orientation-independent, nongeometric-mean measures of seismic intensity from two horizontal components of motion. *Bull Seismol Soc Am* 100(4):1830–1835. <https://doi.org/10.1785/0120090400>
- Boore DM, Bommer JJ (2005) Processing of strong-motion accelerograms: needs, options and consequences. *Soil Dynam Earthq Eng* 25(2):93–115. <https://doi.org/10.1016/j.soildyn.2004.10.007>
- Boore DM, Stewart JP, Seyhan E, Atkinson G (2013) NGA-West 2 equations for predicting response spectral accelerations for shallow crustal earthquakes. PEER Report 2013/05. Pacific Earthquake Engineering Research Center, Berkeley, California
- Boore DM, Stewart JP, Seyhan E, Gail MA (2014) NGA-West2 equations for predicting PGA, PGV, and 5% damped PSA for shallow crustal earthquake. *Earthq Spectra* 30(3):1057–1085. <https://doi.org/10.1193/070113eqs184m>
- Field EH, Arrowsmith RJ, Biasi GP, Bird P, Dawson TE, Felzer KR, Jackson DD, Johnson KM, Jordan TH, Madden C, Michael AJ, Milner KR, Page MT, Parsons T, Powers PM, Shaw BE, Thatcher WR, Weldon RJ, Zeng Y (2014) Uniform California Earthquake Rupture Forecast, Version 3 (UCERF3)—The Time-Independent Model. *Bull Seismol Soc Am* 104(3):1122–1180. <https://doi.org/10.1785/0120130164>
- Graizer V (2018) GK17 ground-motion prediction equation for horizontal PGA and 5% damped PSA from shallow crustal continental earthquakes. *Bull Seismol Soc Am* 108(1):380–398. <https://doi.org/10.1785/0120170158>
- Graizer V (2022) Geometric spreading and apparent anelastic attenuation of response spectral accelerations. *Soil Dynam Earthq Eng* 162:107463. <https://doi.org/10.1016/j.soildyn.2022.107463>
- Graves RW, Aagaard BT, Hudnut KW, Star LM, Stewart JP, Jordan TH (2008) Broadband simulations for mw 7.8 southern San Andreas earthquakes: Ground motion sensitivity to rupture speed. *Geophys Res Lett* 35:L22302. <https://doi.org/10.1029/2008GL035750>
- Kaklamanos J, Baise LG, Boore DM (2011) Estimating unknown input parameters when implementing the NGA ground-motion prediction equations in engineering practice. *Earthq Spectra* 27(4):1219–1235. <https://doi.org/10.1193/1.3650372>
- Olsen KB, Day SM, Minster JB, Cui Y, Chourasia A, Faerman M, Moore R, Maechling P, Jordan T (2006) Strong shaking in Los Angeles expected from southern San Andreas earthquake. *Geophys Res Lett* 33:L07305. <https://doi.org/10.1029/2005GL025472>
- Petersen MD, Moschetti MP, Powers PM, Mueller CS, Haller KM, Frankel AD, Zeng Y, Rezaeian S, Harnsen SC, Boyd OS, Field N, Chen R, Rukstales KS, Luco N, Wheeler RL, Williams RA, Olsen AH (2014) Documentation for the 2014 update of the United State national seismic hazard maps. Open-File Rep 2014–1091, USGS.


- Rodriguez-Marek A, Montalva GA, Cotton F, Bonilla F (2011) Analysis of single-station standard deviation using the KiK-net data. *Bull Seismol Soc Am* 101(3):1242–1258. <https://doi.org/10.1785/0120100252>
- Seyhan E, Stewart JP (2014) Semi-empirical nonlinear site amplification from NGA-West2 data and simulations. *Earthq Spectra* 30(3):1241–1256. <https://doi.org/10.1193/063013EQS181M>
- Shahi SK, Baker JW (2011) An empirically calibrated framework for including the effects of near-fault directivity in probabilistic seismic hazard analysis. *Bull Seismol Soc Am* 101(2):742–755. <https://doi.org/10.1785/0120100090>
- State Administration for Market Regulation, China National Standardization Administration Committee (2020) GB/T 17742–2020 the Chinese seismic intensity scale. China Standards, Beijing. (in Chinese)
- Wang W, Hao J, Yao Z (2013) Preliminary result for rupture process of Api. 20, 2013, Lushan earthquake, Sichuan, China. *Chin J Geophys* 56(4):1412–1417. <https://doi.org/10.6038/cjg20130436> (in Chinese)
- Wen RZ, Ren YF (2014) Strong-motion observations of the Lushan earthquake on 20 April 2013. *Seismol Res Lett* 85(5):1043–1055. <https://doi.org/10.1785/0220140006>
- Wen RZ, Xu PB, Wang HW, Ren YF (2018) Single-station standard deviation using strong-motion data from Sichuan Region, China. *Bull Seismol Soc Am* 108(4):2237–2247. <https://doi.org/10.1785/0120170276>
- Wills CJ, Petersen M, Bryant WA, Reichle M, Saucedo GJ, Tan S, Taylor G, Treiman J (2000) A site-conditions map for California based on geology and shear-wave velocity. *Bull Seismol Soc Am* 90(6B):S187–S208. <https://doi.org/10.1785/0120000503>
- Xie JJ, Wen ZP, Li XJ, Li YQ, Lu HS, Huang JY (2012) Analysis of velocity pulses for near-fault strong motions from the Wenchuan earthquake based on wavelet method. *Chin J Geophys* 55(6):1963–1972. <https://doi.org/10.6038/j.issn.0001-5733.2012.06.017> (in Chinese)
- Xie JJ, Zimmaro P, Li XJ, Wen ZP (2017) Rupture Directivity effects on strong ground motion during the 15 April 2016 7.0 Kumamoto Earthquake in Japan. *Bull Seismol Soc Am* 107(3):1265–1276. <https://doi.org/10.1785/0120160258>
- Xie JJ, Li XJ, Wen ZP, Jia L, An Z, Cui J, Lin G, Zhang Q, Jiang P, Xie Q, Wang P, Zimmaro P, Stewart JP (2022) Soil Profile Database and Site classification for National strong-motion stations in Western China. *Seismol Res Lett* 93(3):1930–1942. <https://doi.org/10.1785/0220210271>
- Xu PB, Ren YF, Wen RZ, Wang HW (2020) Observations on regional variability in ground-motion amplitude from six  $M_w \sim 6.0$  earthquakes of the north-south seismic zone in China. *Pure Appl Geophys* 177(1):247–264. <https://doi.org/10.1007/s00024-019-02176-6>
- Yi GX, Long F, Liang MJ, Zhao M, Zhang HP, Zhou RJ, Li Y, Liu H, Wu P, Wang SW, Li J, Wu WW, Su JR (2023) Seismogenic structure of the 5 September 2022 Sichuan Luding  $M_S$  6.8 earthquake sequence. *Chin J Geophys* 66(4):1363–1384. <https://doi.org/10.6038/cjg2023Q0923> (in Chinese)
- Zhang X, Feng W, Xu L, Li C (2017) The source-process inversion and the intensity estimation of the 2017  $M_S$  7.0 Jiuzhaigou earthquake. *Chin J Geophys* 60(10):4105–4116. <https://doi.org/10.6038/cjg20171035> (in Chinese)
- Zhang B, Yu YX, Li XJ, Wang YS (2022) Ground motion prediction equation for the average horizontal component of PGA, PGV, and 5% damped acceleration response spectra at periods ranging from 0.033 to 8.0 s in southwest China. *Soil Dynam Earthq Eng* 159:107297. <https://doi.org/10.1016/j.soildyn.2022.107297>
- Zhang L, Zhou Y, Zhang X, Zhu A, Li B, Wang S, Liang S, Jiang C, Wu J, Li Y, Su J, Yan L, Fang L (2023) 2022  $M_w$  6.6 Luding, China, Earthquake: a strong Continental Event Illuminating the Moxi Seismic Gap. *Seismol Res Lett* 94:2129–2142. <https://doi.org/10.1785/0220220383>

**Publisher's Note** Springer Nature remains neutral with regard to jurisdictional claims in published maps and institutional affiliations.

Springer Nature or its licensor (e.g. a society or other partner) holds exclusive rights to this article under a publishing agreement with the author(s) or other rightsholder(s); author self-archiving of the accepted manuscript version of this article is solely governed by the terms of such publishing agreement and applicable law.



## Authors and Affiliations

Bin Zhang<sup>1,2</sup> · Xiaojun Li<sup>3</sup>  · Yanxiang Yu<sup>4</sup> · Xiaojian Lu<sup>1</sup> · Mianshui Rong<sup>3</sup> · Su Chen<sup>3</sup> · Zhao An<sup>4</sup> · Zhenghui Xiong<sup>5</sup>

---

✉ Xiaojun Li  
beerli@vip.sina.com

<sup>1</sup> Institute of Earthquake Forecasting, China Earthquake Administration, Beijing 100036, China

<sup>2</sup> Institute of Geomechanics, Chinese Academy of Geological Sciences, Beijing 100081, China

<sup>3</sup> Key Laboratory of Urban Security and Disaster Engineering of China Ministry of Education, Beijing University of Technology, Beijing 100124, China

<sup>4</sup> Institute of Geophysics, China Earthquake Administration, Beijing 100081, China

<sup>5</sup> Unicom Digital Technology Co., Ltd, Beijing 100032, China